IEEE Access
Multidisciplinary | Rapid Review | Open Access Journal

Received 10 March 2024, accepted 24 March 2024, date of publication 2 April 2024, date of current version 9 April 2024.

Digital Object Identifier 10.1109/ACCESS.2024.3382713

RESEARCH ARTICLE

Graphene-Metamaterial Based Tunable Broadband Polarization Insensitive Absorber for Terahertz Antenna Design

RUMMANUR RAHAD, (Member, IEEE), ABU S. M. MOHSIN, (Member, IEEE), MOHAMMED BELAL HOSSAIN BHUIAN, AND MD. MOSADDEQUR RAHMAN

Department of Electrical and Electronic Engineering, Optics and Photonics Research Group, BRAC University, Dhaka 1212, Bangladesh

Corresponding author: Abu S. M. Mohsin (asm.mohsin@bracu.ac.bd)

This work was supported by BracU Research Seed Grant Initiate under Grant RSGI 2023.

ABSTRACT The advent of graphene has opened new avenues for the design of high-performance metamaterial devices, particularly in the realm of electromagnetic absorption applications. This paper introduces a novel design for a broadband tunable graphene metamaterial absorber (GMMA) utilizing graphene. Through numerical simulations, our proposed GMMA demonstrates an absorption bandwidth of 3 THz (1.14 – 4.14 THz) with absorptivity exceeding 90% for both transverse magnetic (TM) and transverse electric (TE) modes. A comprehensive numerical analysis, using a transmission line equivalent circuit model, has been proposed to find out the impedance components of all the corresponding layers, which can be significant to determine the impedance matching. The absorber exhibits wideband tunability, polarization insensitivity, and robust tolerance to structural variations, making it a promising candidate for diverse applications in the terahertz (THz) band especially in the antenna regime. Our proposed GMMA antenna can achieve a gain of 37.48 dB, a directivity of 32.81 dB, a return loss of -34 dB, and an efficiency of 99.96%. This research provides a valuable contribution to the development of tunable broadband GMMAs for THz frequencies, addressing the increasing demand for high-speed and efficient devices in the modern era of science and technology.

INDEX TERMS Graphene-metamaterial absorber, terahertz antenna, absorptivity, bandwidth, gain, directivity, efficiency.

I. INTRODUCTION

Metamaterials (MMs) are materials that are artificially designed to have special properties [1], [2]. The term ''metamaterials'', coined by Walser in 2001, refers to a class of materials that exhibit exceptional properties beyond those of their conventional equivalents [3]. MMs can take the form of regularly built macroscopic composites in two or three dimensions that exhibit unique features ranging from microwave to optical frequencies. MM research extends its influence across diverse domains such as electromagnetics, optics, optoelectronics, and solid-state physics. The inception of significant breakthroughs in MM studies traces back to 1968 when Veselago pioneered the concept of materials exhibiting a negative refractive index (NRI) characterized by $\varepsilon, \mu < 0$ [4]. With the continuous evolution of MMs, a rich array of innovative MMs has undergone exploration, including water-based MM [5], graphene-based MM [6], VO_2-based MM [7], perovskite-coated MM [8], and so on. This symphony of MM diversity has given rise to a captivating ensemble of applications, encompassing not only modulators [9] and sensors [10] but also venturing into the

The associate editor coordinating the review of this manuscript and approving it for publication was Qi Luo.

realm of absorbers. For example, Baqir et al. investigated a hyperbolic metamaterial (HMM)-based optical biosensor for early-stage cancer detection [11].

To achieve absorbers that are simple and compact, the research focus shifted to metamaterial-based absorbers (MMAs). MMAs have thin layers and low density, and they can absorb a high amount of incident electromagnetic (EM) wave. MMAs can trap the EM wave at some specific points in the device and then convert the EM into heat [12]. The inverse Doppler effect, negative refractive index, perfect lensing, left-handed behavior, EM wave cloaking, and perfect absorption are some of these characteristics that are lacking in conventional materials [12], [13], [14], [15]. MMAs have their origins in the seminal work of Landy et al., which highlighted their compact size and thin thickness relative to traditional absorbers [16]. Since then, several improved absorber designs have been developed, but producing a multiband MMA with high efficiency is still a difficult task, and unstable absorption conditions are a common occurrence. A thorough analysis of the literature reveals recurring problems that call for a methodical approach to designing an ideal MMA. These problems include increasing the number of absorption bands, improving working conditions, creating polarization-tunable absorbers, and choosing the best materials for real-world applications [12].

MMAs, as avant-garde MM entities, have attracted widespread attention for their expansive utility. These novel devices transcend traditional boundaries, finding applications as sophisticated sensors [17], integral components of cutting-edge detection systems [18], and keystones in the architecture of high-resolution imaging devices [19]. The exploration and validation of MMs, coupled with the utilization of THz spectroscopy, have emerged as a burgeoning focal point in contemporary research [20]. For the inherent challenge of identifying efficient absorption materials in the THz spectrum from nature, the strategic design of THz MMAs becomes particularly pivotal. Over recent years, an abundance of studies has surfaced, detailing MMAs that find application in EM stealth, detection, modulation, imaging and so on [21]. THz waves, constituting a segment within the EM spectrum, present a practical challenge for direct accessibility, requiring measurement through the periodic properties of either wavelength or energy. Significantly, the penetration depth of THz radiation falls between that of microwaves and infrared waves. However, their limited utility in telecommunications arises due to their absorption by water vapor in the earth's atmosphere. Despite this limitation, THz waves have become a focal point of interest for researchers and scientists in recent years. One noteworthy advantage is the non-ionizing nature of THz waves, a phenomenon that has contributed to their appeal in various research and scientific pursuits [4]. Notably, approaches to achieving tunable MMAs encompass a spectrum of methods, ranging from mechanical adjustments, and laser interventions to temperature manipulation, and voltage modulation [22]. THz absorbers hold a significant position within the realms of emitters, sensors, photodetectors, and photovoltaic applications [23]. The evolution of MMA design, elucidated by Landy et al., has paved the way for an innovative approach that seamlessly extends from microwaves to the intricate domains of THz and visible light [24]. Cai et al. proposed dynamically controlling THz wave-fronts by rotating layers in a cascaded meta-device, showcasing proof-of-concept devices [25]. This pioneering method has sparked considerable interest, capturing the attention of researchers and enthusiasts alike, thereby catalyzing an intensified focus on the meticulous design of THz absorbers.

In the realm of material science, the relentless pursuit of advancements has spotlighted graphene, a material distinguished by its extraordinary mechanical, electrical, and optical properties. In the current landscape of scientific exploration, an innovative technique has emerged, centered around the utilization of graphene in conjunction with an external bias voltage to strategically fine-tune the absorption characteristics of THz MMAs [22]. This single-layer, two-dimensional array of carbon atoms arranged in a hexagonal lattice has emerged as a pivotal player in the design of nano-devices with unprecedented efficiencies. Geim and his group's seminal discovery of graphene in 2004 opened new avenues, particularly in the exploration of two-dimensional thin film materials [26]. Graphene's prowess extends beyond its mechanical and electrical attributes; it proves to be an ideal 2D medium capable of supporting surface plasmons (SPs) in the infrared and THz regions. This unique quality facilitates robust sub-wavelength confinement of EM fields, positioning graphene as a suitable medium for the creation of MMA that achieve perfect absorption in the infrared and THz domains [27]. Moreover, graphene's versatility comes to the forefront in optical and THz systems, where its conductivity can be dynamically controlled by external DC-bias voltage. This characteristic not only enhances performance but also allows for a reduction in device dimensions [28]. Zhong et al. explored laser-induced graphene (LIG) for creating superhydrophobic structures with applications in deicing and anti-icing [29]. Baqir et al. examined filtering aspects of a graphene bilayer-coated substrate with embedded nanorods, revealing high transmission and stop bands for specific frequencies [30]. The autonomous absorption process of graphene, coupled with the phenomenon of destructive interference, contributes to absorption levels nearing unity.

Hence, the exploration of fewer-layer MMAs featuring a two-dimensional periodic array of patterned graphene has emerged as a pivotal research focus for achieving optimal absorption, wide bandwidth, and remarkable tunability [31]. Notably, Huang et al. introduced a broadband MMA employing a graphene sheet with a specific pattern, achieving absorption exceeding 90% at 1.57 THz [32] Liao et al. proposed a ultra-broadband absorber with a bandwidth range of 0.75-1.73 THz over 90% absorption [33]. Li et al.

demonstrated a metasurface that exhibited a absorptivity of over 90% in the range of 0.67 THz-0.95 THz [34]. Lu et al. took a different approach by patterning graphene into a discrete periodic structure to attain wide bandwidth absorption [31]. Pan et al. demonstrated another THz metamaterial rasorber (MSR) obtained absorption (over 0.88%) at 1.46–2.29 THz [35]. Pan et al. proposed another MSR with bandwidth range of 2–3.08 THz (42.5%) [36]. Ma et al. proposed the ultra-wideband absorption and the transmission window in the absorption band [37]. The research landscape in the THz regime has witnessed the proposition of numerous patterned graphene-based MA structures designed for both narrowband and broadband absorption [31], [32], [38]. Despite these strides, it is emphasized in the passage that the pursuit of bandwidth enhancement for MMAs, especially those incorporating graphene, is still at a nascent stage of exploration.

In this paper, a graphene-structured metamaterial absorber (GMMA) is introduced, and a broadband spectrum with a bandwidth of 3 THz is achieved over 90% efficiency, spanning from 1.14 THz to 4.14 THz. We propose a precise equivalent circuit model, offering a seamless integration into simulation programs for comprehensive analysis within integrated circuit frameworks. This methodology enables the fine-tuning and broadening of the frequency range of the efficient response through the manipulation of graphene gate voltage, showcasing the adaptability and versatility of GMMAs. The study explores the utilization of GMMA to optimize THz EM wave capture and transmission. By overcoming challenges through graphene's unique properties, the GMMA antenna demonstrates enhanced performance in terms of gain, directivity, return loss, and efficiency for efficient THz communication.

II. STRUCTURAL DESIGN AND METHODOLOGY

In Fig. 1(a), the top view of GMMA's unit cell is depicted, while Fig. 1(b) presents the three-dimensional structure of the proposed GMMA (The evolution of GMMA structure and optimization is illustrated in supplemental 1). The absorber comprises two distinct layers: the upper layer features a graphene pattern, and the lower layer is composed of a dielectric layer made of SiO_2, which exhibits a relative permittivity (ε) of 2.25 with negligible loss [39]. The refractive index of SiO_2 in the 1 THz to 10 THz range varies from about 1.44 to 1.55, depending on the wavelength and the temperature. These values may vary depending on the purity and crystallinity of the SiO_2 sample. SiO_2, which exerts minimal impact on the performance of the absorber, is employed as the substrate to provide support for the absorber. SiO_2 can minimize circuit capacitance and dielectric losses, which enhances signal quality and transmission speed. It also resists moisture absorption and has high thermal stability, protecting the electrical performance from variations in humidity and temperature [40]. Additionally, it exhibits minimal dielectric dispersion, meaning that its dielectric constant remains relatively constant at various frequencies [41]. The thickness of the SiO_2 and graphene layers is denoted by t_s and t_g, respectively, as illustrated in Fig. 1(d). The optimal unit cell size of GMMA is $P\,\mu\text{m} \times P\,\mu\text{m}$ (where $P = 4.5\,\mu\text{m}$).

The working principle of our proposed absorber is based on the impedance matching and destructive interference conditions [42]. Impedance matching means that the input impedance of the metasurface is equal to the characteristic impedance of the medium, which ensures that there is no reflection of the incident wave. Destructive interference means that the transmitted wave from the metasurface is canceled out by the reflected wave from the ground plane, which ensures that there is no transmission of the incident wave. Therefore, the incident wave is fully absorbed by the metasurface and converted into other forms of energy, such as heat or electricity [42]. In the presence of light, the entirety depicted in Fig. 1(a) operates collectively, triggering the excitation, and yielding a photoconductor that mimics the characteristics of an absorber. In absorption mode, when the conductivity rises and the surface pattern matches free space impedance, incoming EM plane waves generate current within the device. The generated current results from two components along the u and v axes, derived by a 45° counterclockwise rotation of the x and y axes. Due to distinct geometric characteristics in the u and v directions, the pattern exhibits varied impedance to EM waves. For TE case, the incident wave E_{in} along the y-axis can be expressed as Eq. 1.

$$E_{in} = E_y i_y = E_u i_u + E_v i_v \tag{1}$$

The reflected wave E_{r} can be expressed as Eq. 2 from Fig. 1 (c) [33].

$$E_{\mathbf{r}} = \begin{pmatrix} i_u & i_v \end{pmatrix} \begin{pmatrix} r_{uu} & r_{uv} \\ r_{vu} & r_{vv} \end{pmatrix} \begin{pmatrix} E_u \\ E_v \end{pmatrix} \tag{2}$$

The co-polarized reflection coefficients r_{uu} and r_{vv} can be expressed as Eqs. 3 and 4.

$$r_{uu} = |r_{uu}| e^{j\phi_u} \tag{3}$$

$$r_{vv} = |r_{vv}| e^{j\phi_v} \tag{4}$$

In this way, the modified Eq. 2 will be:

$$E_{\mathbf{r}} = i_u r_{uu} E_u + i_v r_{vv} E_v = E_y \cos(45^\circ)(i_u r_{uu} + i_v r_{vv}) \tag{5}$$

If $|\mathbf{r}_{uu}| = |\mathbf{r}_{vv}|$ and $\Delta\phi = \phi_v - \phi_u = \pi + 2k\pi,\ k \in \mathbb{Z}$ can be satisfied, then Eq. 2 can be more simplified, and the polarization conversion (PC) can be achieved [33].

$$E_{\mathbf{r}} = E_y \cos(45^\circ) e^{j\phi_u} (i_u + i_v e^{j\Delta\phi}) |r_{uu}| = i_x |r_{uu}| e^{j\phi_u} E_y \tag{6}$$

The PC rate can be expressed expressed by the following Eq. 7 [33], [34]:

$$\text{PCR} = \frac{r_{xy}^2}{r_{xy}^2 + r_{yy}^2} \tag{7}$$

Here, r_{xy} and r_{yy} can be expressed as Eq. 8 and Eq. 9 respectively:

$$r_{xy} = \frac{|E_{xr}|}{|E_{yi}|} \tag{8}$$

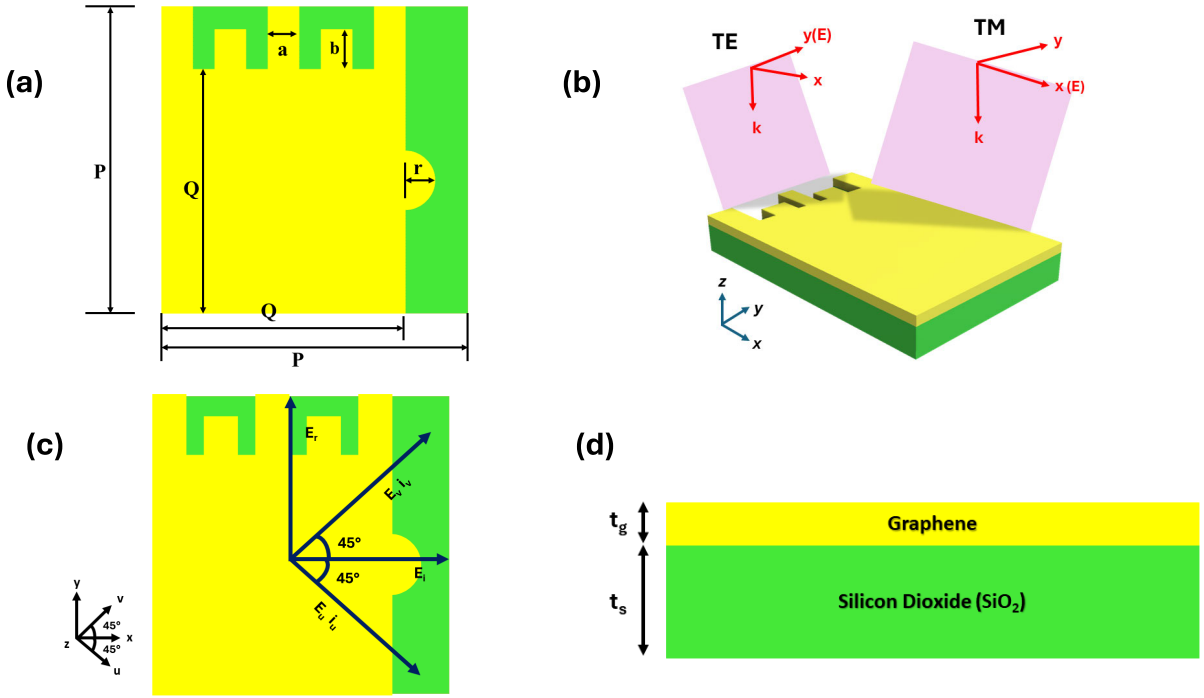

FIGURE 1. (a) Top view of the unit cell, (b) Isometric view of the unit cell with TM and TA waves, (c) Unit cell with incident and reflected polarized EM wave. and (d) Side view of the unit cell (SiO_2 = 'green layer' and Graphene = 'yellow layer').

$$r_{yy} = \frac{|E_{yr}|}{|E_{yi}|} \tag{9}$$

Here, E_{yi} denotes the E_{in} with polarization in the y-direction, while E_{yr} and E_{xr} represent the E_r in the y- and x-directions, respectively. Hence, the reflectivity (R) can be expressed by the following equation:

$$R = |r_{xy}|^2 + |r_{yy}|^2 \tag{10}$$

Therefore, the absorptance can be calculated using the following equations [34]:

$$A = 1 - R - T \tag{11}$$

Here, the consideration of transmittance in the absorption calculation was omitted due to the inhibitory effect of the substrate of the absorber. The inhibitory effect of the substrate of the absorber means that the substrate prevents or reduces the transmission of EM waves through the absorber [43]. Therefore, the simplified absorptance formula can be expressed by the following equation [34]:

$$A = 1 - R = 1 - |r_{xy}|^2 - |r_{yy}|^2 \tag{12}$$

Absorption is the process of converting EM energy into heat or other forms of energy within a material. One way to describe absorption is in terms of surface current densities, which are the currents flowing on the surface of a material. Surface current densities can be induced by an incident EM wave, and they produce a secondary EM wave that interferes with the incident wave. The interference can result in reflection, transmission, or absorption of the wave, depending on the properties of the material and the angle of incidence. The amount of absorption can be calculated by using the Poynting vector, which represents the power flow of an EM wave. The Poynting vector is given by $\mathbf{S} = \mathbf{E} \times \mathbf{H}$, where $\mathbf{E}$ is the electric field and $\mathbf{H}$ is the magnetic field. The absorption per unit area is then given by $A = -\frac{1}{2}\mathrm{Re}(\mathbf{K}^* \cdot \mathbf{E})$, where $\mathbf{K}$ is the surface current density and Re denotes the real part. This formula shows that the absorption depends on the magnitude and phase of the surface current density relative to the electric field of the incident wave. To accurately model the EM behavior, open boundary conditions were implemented along the z-direction, ensuring that the simulation space extends infinitely in that direction. Meanwhile, periodic boundary conditions were employed along the x and y directions, facilitating a periodic repetition of the simulation unit in those dimensions. These choices in boundary conditions contribute to a comprehensive representation of the EM interactions within the simulated environment, enhancing the accuracy of the results obtained through the simulation. This research delves into the intricate dynamics of TE waves in the context of EM interactions. TE waves, characterized by their perpendicular orientation to the propagation direction, play a crucial role in the study. The investigation focuses on the x-z incident plane, with specific attention to the azimuthal angle ϕ, set at 0°, defining the orientation of the incident TE wave within the x-y plane. The permittivity of graphene (ε_g) can be expressed by the following equation [44]:

$$\varepsilon_g = 1 + j\frac{\sigma(\omega)}{\varepsilon_0 \omega t_g} \tag{13}$$

where, ω represents the angular frequency, t_g denotes the thickness of graphene layer, and ε_0 stands for the permittivity in a vacuum environment. The surface conductivity of graphene, denoted as $\sigma(\omega)$, is typically a combination of intra-band conductivity and inter-band conductivity. In the THz to optical frequency range, the complex surface conductivity $\sigma(\omega)$ of graphene can be characterized by Kubo formula [45]:

$$\begin{aligned}&\sigma(\omega, \mu_c, \Gamma, T)\\&= \sigma_{\text{intra}}(\omega, \mu_c, \Gamma, T) \quad + \sigma_{\text{inter}}(\omega, \mu_c, \Gamma, T)\\&= -\frac{ie^2k_BT}{\pi\hbar^2}\left[\frac{1}{(\omega+i2\Gamma)^2}\int_0^\infty d\epsilon\left(\frac{\delta n_F(\epsilon)}{\delta\epsilon}-\frac{\delta n_F(-\epsilon)}{\delta\epsilon}\right)\epsilon\right]\\&\quad -\frac{ie^2k_BT}{\pi\hbar^2}\left[\int_0^\infty d\epsilon\frac{n_F(-\epsilon)-n_F(\epsilon)}{(\omega+i2\Gamma)^2-4\left(\frac{\epsilon}{\hbar}\right)^2}\right]\end{aligned} \tag{14}$$

where, σ_{intra} and σ_{inter} respectively stand for intra-band and inter-band conductivities, signifying the conductivity within a specific energy band and between different energy bands. The symbol e represents the elementary charge of an electron, while $\hbar$ denotes the reduced Planck's constant in quantum mechanics, ϵ refers to the energy of the charge carriers, typically electrons, k_B is Boltzmann constant and ω represents the radian frequency in wave-related contexts. Additionally, $\Gamma = 5\text{meV}$ signifies the charged particle scattering rate, indicating the rate at which charged particles experience scattering, with a specific value of 5 meV, the temperature $T = 300\text{K}$ is specified as room temperature in Kelvin [45], [46] and n_F is the Fermi-Dirac distribution function,

$$n_F(\epsilon) = \frac{1}{1+\exp\left(\frac{k_BT(\epsilon-\mu_c)}{k_BT}\right)} \tag{15}$$

where μ_c denotes the chemical potential of graphene. This equation describes the probability of finding a fermion with energy ϵ in a system at temperature T, taking into account the chemical potential μ_c and the Boltzmann constant k_B. In equation 14, the approximate value of σ_{intra} and σ_{inter} can be calculated analytically by the following equations [46], [47]:

$$\begin{aligned}&\sigma_{\text{intra}}(\omega, \mu_c, \Gamma, T)\\&\approx i\frac{e^2k_BT}{\pi\hbar(\omega+i2\Gamma)}\left[\frac{\mu_c}{k_BT}+2\ln\left(e^{-\frac{\mu_c}{k_BT}}+1\right)\right]\end{aligned} \tag{16}$$

$$\begin{aligned}&\sigma_{\text{inter}}(\omega, \mu_c, \Gamma, T)\\&\approx i\frac{e^2}{4\pi\hbar}\ln\left[\frac{2|\mu_c|-(\omega+i2\Gamma)\hbar}{2|\mu_c|+(\omega+i2\Gamma)\hbar}\right]\end{aligned} \tag{17}$$

Equation (17) holds true when k_BT is significantly smaller than both $|\mu_c|$ and $\hbar\omega$. When graphene is subject to an external load with a controlled voltage V_A, its chemical potential μ_c can be approximated using the subsequent formula,

$$|\mu_c| \approx \hbar v_F\,(\pi a_0|V_A - V_{\text{Dirac}}|)^{1/2} \tag{18}$$

where the Fermi velocity of the Dirac fermions is approximately $v_F = 9\times10^5$ m/s, the constant determined using a single capacitor model is $a_0 \approx 9\times10^{16}\,\text{m}^{-2}\,\text{V}^{-1}$, and the Dirac voltage offset induced by natural doping is $V_{\text{Dirac}} = 0.8\,\text{V}$ [46], [47]. The dielectric constant for different values of chemical potential (0.2 eV – 0.7 eV) has been illustrated in Fig. 2.

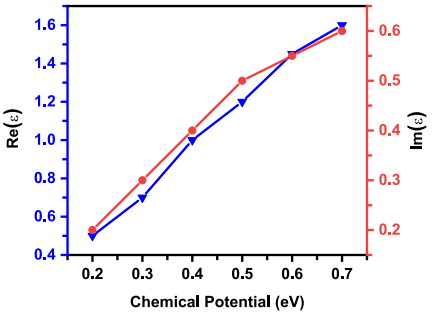

FIGURE 2. Dielectric constant for different values of chemical potential of the proposed GMMA.

In the THz band, the intra-band conductivity prevails when the photon energy, $\hbar\omega$, is much smaller than twice the Fermi energy ($2E_f$). In accordance with Pauli's exclusion principle, the inter-band conductivity can be neglected under these conditions [47], leading to the modified equation:

$$\sigma_{\text{inter}}(\omega, \mu_c, \Gamma, T) \approx \sigma_{\text{intra}}(\omega, \mu_c, \Gamma, T) \tag{19}$$

The relationship between carrier density and the conductivity of graphene can be articulated as follows [48]:

$$n_s = 2\frac{\pi\hbar^2}{e^2}\int_0^\infty \varepsilon[f(\varepsilon)-f(\varepsilon+2\mu_c)]d\varepsilon \tag{20}$$

The surface impedance (Z_g) of graphene is expressed as follows [49]:

$$Z_g = \frac{1}{\sigma_g} \tag{21}$$

where σ_g is the surface conductivity of the graphene.

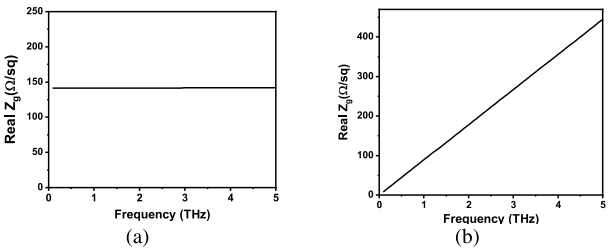

FIGURE 3. Results from numerical calculations depict the (a) real part and (b) imaginary part of the surface impedance of graphene.

We used numerical calculations to calculate the real and imaginary components of the surface impedance of the graphene throughout the examined frequency range, as shown in Fig. 3, while taking into account a predetermined relaxation period and temperature. For our case, graphene's chemical potential coincides with a decrease in both the real

and imaginary components of surface impedance. Notably, the real component remains constant as frequency increases, but the imaginary component consistently rises as frequency increases. It is critical to emphasize the significant changes in the surface impedance of the graphene layer for different values of μ_c. Manipulation is possible by modifying the gate voltage, which influences the surface impedance of the patterned graphene and, as a result, the performance of the proposed GMMA. As a result, graphene appears as a suitable material for fabricating THz devices due to its extraordinary tunability. The comprehensive absorbance characteristics of the suggested structure can be elucidated through the effective medium theory [50]. Illustrated in Fig. 4, we explored the real and imaginary components of the effective impedance of the proposed MA within the investigated frequency range using the equation [51]:

$$z = \sqrt{\frac{(1+S_{11})^2 - S_{21}}{(1-S_{11})^2 - S_{21}}} = \frac{1+S_{11}}{1-S_{11}} \tag{22}$$

Here, S_{11} and S_{21} represent the S-parameters derived from simulations. In the broad frequency span of 1.14-4.14 THz, the real and imaginary segments of the effective impedance shown in Fig. 4. This outcome signifies outstanding impedance matching between the proposed MA and free space. Consequently, near-perfect absorption of the proposed MA is attained within this frequency band [52].

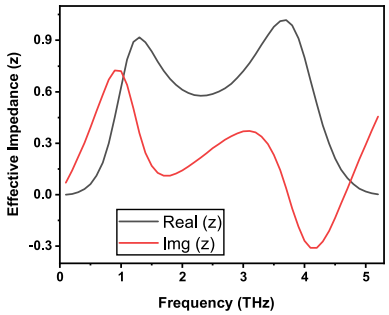

FIGURE 4. Real and imaginary part of the effective impedance of the proposed GMMA.

The propagation constant of the EM wave in a graphene-vacuum configuration is [53]:

$$\beta = \frac{k_0}{\sqrt{1 - \left(\frac{2}{Z_0\sigma}\right)^2}} \tag{23}$$

where k_0 represents the wave vector of the incident wave, while Z_0 denotes the vacuum impedance.

III. EQUIVALENT CIRCUIT MODEL OF GMMA

The theoretical framework for the proposed structure is elucidated through the transmission line perspective, delineated in the context of its equivalent circuit [4], [54]. According to Fig. 5(a), the GMMA's equivalent circuit is divided into

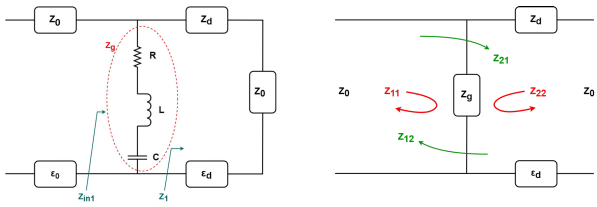

FIGURE 5. (a) Equivalent circuit model of the GMMA, (b) equivalent hypothetical 2-ports network system.

three separate impedance sections. The process begins in free space, which refers to the air, and is defined by an intrinsic impedance denoted as $Z_0 \approx 377\,\Omega$ [55]. This intrinsic impedance arises due to the propagation of THz waves that originate in the air. As the waves progress, their path intersects with the graphene impedance $Z_g(f)$. This interaction results in the manifestation of an RLC (resistor-inductor-capacitor) resonator within the equivalent circuit. In essence, the characteristics of the graphene impedance become apparent as the waves engage with it, shaping the behavior of the overall circuit. Afterward, the impedance of the dielectric spacer, functioning like a short transmission line, is denoted as Z_d, contingent upon the permittivity of the dielectric material SiO_2. The characterization of graphene layers as a parallel element stems from their extremely thin thickness relative to THz wavelengths. The noteworthy aspect here is that the graphene layers are so thin that they can be conceptualized as parallel structures in relation to the longer THz wavelengths [56], [57], [58], [59]. By referring to Fig. 5(a), it is possible to determine an equivalent impedance to the dielectric spacer based on the specific dielectric chosen for our structure. Furthermore, considering the resonance characteristics of graphene at a particular frequency, it becomes possible to incorporate a branch into the diagram that symbolizes the presence of the RLC layer. The following equations provide the values for all impedances shown in Fig. 5(a) [4]:

$$Z_g(f) = R_g(f) + jX_g(f) = R_g(f) + j\left(2\pi f L_g - \frac{1}{2\pi f C_g}\right), Z_g(f) = \frac{1}{\sigma_g(f)} \tag{24}$$

$$Z_1(f) = jZ_d \tan(T_1 k_d) \tag{25}$$

$$k_d(f) = 2\pi f\sqrt{\epsilon_0\epsilon_d\mu_0} \tag{26}$$

$$Z_d = \sqrt{\frac{\mu_0}{\epsilon_0\epsilon_d}} \tag{27}$$

here, $Z_1(f)$ represents the input surface impedance and $k_d(f)$ is the wave number. The electrical length of the structure, denoted as $T_1 k_d$, is equivalent to 0.7192 radians, progressing from the short circuit to the source. In the configuration depicted in Fig. 5(a), $Z_{\text{in}1}(f)$ is contingent upon the impedance of graphene ($Z_g(f)$) and the dielectric spacer, characterized as a short transmission line, as well as the

impedances associated with free space (Z_d, Z_0).

$$Z_1(f) = Z_d \frac{Z_0 + jZ_d \tan(T_1 kd)}{Z_d + jZ_0 \tan(T_1 kd)} \tag{28}$$

The calculation of $Z_{\text{in}}(f)$ involves matrix expressions:

$$\begin{bmatrix} P_1 & Q_1 \\ R_1 & S_1 \end{bmatrix} = \alpha\beta\gamma \tag{29}$$

where,

$$\alpha = \begin{bmatrix} 1 & 0 \\ \frac{1}{Z_g(f)} & 1 \end{bmatrix}, \beta = \begin{bmatrix} \cos(T_1 k_d) & jZ_d \sin(T_1 k_d) \\ j\sin(T_1 k_d) & Z_d \cos(T_1 k_d) \end{bmatrix},$$
$$\gamma = \begin{bmatrix} \cos(\text{FSEL}) & jZ_0 \sin(\text{FSEL}) \\ \frac{j\sin(\text{FSEL})}{Z_0} & \cos(\text{FSEL}) \end{bmatrix} \tag{30}$$

Here, α represents the transmission matrix of the graphene layer, β denotes the transmission matrix of the SiO_2 layer, and γ signifies the transmission matrix of free space. The relationship between the scattering matrix and the transmission matrix can be illustrated by Equation (31), as shown at the bottom of the next page. Here, the free space electrical length, symbolized by 'FSEL', serves as a measure of the distance traveled by a signal within the free space medium. It characterizes the phase shift experienced by the signal as it propagates through the open space, providing insight into the spatial aspect of the EM wave's journey in a vacuum or unobstructed environment.

Transmission matrix formulas can be employed, and in this method, we describe the ABCD matrix by customizing it for the hypothetical 2-port network. This detailed formulation considers how voltages and currents interact in the network, offering a more nuanced description of its behavior. Consequently, the following relation can be established [60]:

$$\begin{bmatrix} V_1 \\ I_1 \end{bmatrix} = \begin{bmatrix} P_1 & Q_1 \\ R_1 & S_1 \end{bmatrix} \begin{bmatrix} V_2 \\ I_2 \end{bmatrix} \tag{32}$$

Equations (32) allow us to extract the P_1, Q_1, R_1, and S_1 as functions of impedances using the aforementioned relation. We first calculate the transmission matrix equations for the configuration shown in Fig. 5(a) and then use equation (31) to establish the relationship between the transmission matrix and scattering matrix. Finally, we formulate the scattering equation as a function of P_1, Q_1, R_1, S_1, and Z_0. This stage entails a thorough analysis of the system's response to changing parameters, capturing the complex interaction between the scattering and transmission properties.We next apply this analytical method to a theoretical 2-port network and use it to obtain the impedance matrix [61], [62]. In doing so, Z_{11}, Z_{12}, Z_{21}, and Z_{22} are used to describe P_1, Q_1, R_1, and S_1 in terms that offer a more comprehensive and adaptable depiction of the network's behavior. A greater comprehension of the ways in which the many impedance components contribute to the overall dynamics of the system is made possible by the theoretical foundation of this transformation. To estimate P_1 and R_1 in the particular case shown in Fig. 5(a), where the load impedance Z_L is set to $Z_0 \approx 377\ \Omega$, we use equations (34). Furthermore, we use equation (35) to compute Z_{in1} for this specific example, providing information on the input impedance under the specified circumstances. This meticulous analysis sets the stage for the subsequent application of equation (29), enabling the determination of the values of P_1, Q_1, R_1, and S_1 with a high degree of precision. Moving forward, Fig. 5(b) introduces a 2-port system, and we embark on calculating the transmission matrix in terms of impedance. This step, guided by a systematic approach, elucidates the intricate relationship between the impedance parameters and the transmission characteristics of the system, enhancing our understanding of its behavior in diverse scenarios.

$$P_1 = \frac{Z_{11}}{Z_{22}}, \quad Q_1 = \frac{Z_{11}Z_{22} - Z_{12}Z_{21}}{Z_{21}},$$
$$R_1 = \frac{1}{Z_{21}}, \quad S_1 = \frac{Z_{22}}{Z_{21}} \tag{33}$$

The Z_{in} from the schematic is generally expressed in terms of the transmission matrix as $Z_{\text{in}} = \frac{P_1 Z_L + Q_1}{R_1 Z_L + S_1}$. The elements can be derived from the equation are as follows [4]:

$$P_1 = \frac{Z_{11}}{Z_{21}} = 1, \quad R_1 = \frac{1}{Z_{21}} = \frac{1}{Z_g(f)} \tag{34}$$

Hence, the calculation of Z_{in} is performed as follows:

$$Z_{\text{in}} = \frac{P_1 Z_0 + Q_1}{R_1 Z_0 + S_1} = \frac{P_1}{R_1} = Z_g(f) \tag{35}$$

These values can also be determined using equation (29). Therefore, in accordance with the subsequent relationships:

$$\begin{bmatrix} P_1 & Q_1 \\ R_1 & S_1 \end{bmatrix} = \begin{bmatrix} P_2 & Q_2 \\ \frac{P_2}{Z_g} + R_2 & \frac{Q_2}{Z_g} + S_2 \end{bmatrix} \tag{36}$$

where:

$$P_2 = \cos(T_1 k_d)\cos(FESL) - \frac{Z_d \sin(T_1 k_d)\sin(FESL)}{Z_0},$$
$$Q_2 = j\cos(T_1 k_d) Z_0 \sin(FESL) + jZ_d \sin(T_1 k_d)\cos(FESL),$$
$$R_2 = \frac{j\sin(T_1 k_d)\cos(FESL)}{Z_d} - \frac{j\sin(FESL)\cos(T_1 k_d)}{Z_0},$$
$$S_2 = \cos(T_1 k_d)\cos(FESL) - \frac{Z_0 \sin(T_1 k_d)\sin(FESL)}{Z_d}. \tag{37}$$

This approach allows for the determination of Z_{in} within the equivalent circuit model. In cases of impedance matching, Z_{in} equals Z_0, signifying minimal signal reflection [63], [64].

IV. PARAMETER OPTIMIZATION AND ROBUSTNESS ASSESSMENT

To understand the potential impact of different parameter deviations on the performance of the GMMA, we conducted a simulation-based comprehensive assessment of the structural parameters of the proposed GMMA architecture shown in Fig. 1. The simulation process involved varying key parameters, including Q (ranging from 3 to 4 μm), t_s (ranging from 0.1 to 0.5 μm), r (ranging from 0.4 to 0.6 μm),

and b (ranging from 0.65 to 0.80 μm), to comprehensively explore the bandwidth deviations. The absorption spectra corresponding to variations in different parameters are depicted in Fig. 6 (a-d). In this context, we selected optimized parameters, emphasizing a balance between bandwidth and absorption for our GMMA structure. The optimized values

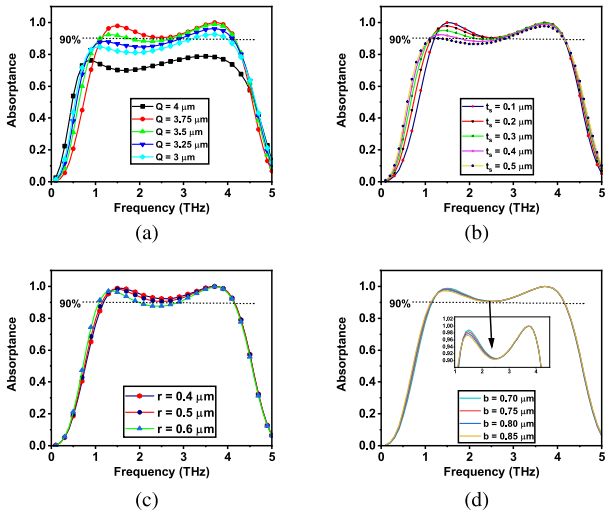

FIGURE 6. Analyzing the absorption spectrum of the suggested GMMA with varying structural parameter.

for GMMA are as follows: $Q = 3.75\,\mu$m, $a = 0.5\,\mu$m, $b = 0.75\,\mu$m, $r = 0.5\,\mu$m, $t_g = 10\,$nm, and $t_s = 0.2\,\mu$m. The parameter (a) has negligible effect on the absorptivity spectra. During the intricate fabrication process of MMs, it is inevitable that certain inaccuracies may arise due to the inherent limitations of the fabrication technology employed [52].

This scrutiny involved an examination of the changes in the bandwidth across various parameter configurations, as detailed in Table 1. To quantify these changes, we utilized the formula:

$$B_{\text{deviation}} = \left(\frac{B_{\text{variable}} - B_{\text{based}}}{B_{\text{based}}}\right) \times 100\%. \qquad (38)$$

Here, B_{based} represents the bandwidth associated with the optimized parameters from the simulation, B_{variable} denotes the bandwidth corresponding to various parameter variations from the simulation, and $B_{\text{deviation}}$ quantifies the percentage deviation between the optimized and simulated bandwidths. This meticulous analysis ensures that the proposed GMMA design maintains robustness in the face of potential fabrication discrepancies, providing valuable insights into the stability and performance resilience of the MM under real-world fabrication conditions. Within the designated ranges of structural parameters, the proposed MMA consistently demonstrates a bandwidth deviation lower than 10%, indicative of its excellent characteristics in the experimental implementation and emphasizing the robustness of its performance across varied conditions [4].

TABLE 1. Comprehensive Study of Bandwidth Deviations in the Proposed GMMA under Different Structural Parameters: Noting Reduction (-) and Increase (+) Signs, and Absorption Efficiency Variation.

Structure Parameter	Value (μm)	BW Deviation (%)	Absorptance
Q	3	+7.35‰	↓
	3.25	+4.75‰	↓
	3.5	+2.35‰	↓
	3.75 (optimized)	-	-
	4	+9.85‰	↓
t_s	0.1	-5.75‰	↑
	0.2 (optimized)	-	-
	0.3	+6.45‰	↓
	0.4	+7.25‰	↓
	0.5	+8.2‰	↓
r	0.4	+1.65‰	↑
	0.5 (optimized)	-	-
	0.6	+4.25‰	↓
b	0.70	-1.85%	↑
	0.75 (optimized)	-	-
	0.80	+1.35‰	↓
	0.85	+1.75‰	↓

V. RESULT AND DISCUSSION

We extensively investigated the dynamic tunability inherent in our proposed GMMA, with the results visualized in Fig. 7(a). By adjusting the chemical potential of the patterned graphene within the range of 0 eV to 0.8 eV, we successfully induced a dynamic shift in the operational characteristics of the structure. This transition seamlessly alternates between absorption and reflection across the entire frequency spectrum and this visual representation depicts the noticeable augmentation in the absorptivity of our designed structure as the chemical potential of the graphene increases. Additionally, the inset in Fig. 7(a) discloses that within the chemical potential range of 0.4 eV to 0.8 eV, the proposed structure consistently maintains absorptivity levels above 90% across a wide bandwidth. For the range where graphene's chemical potential is greater than or equal to 0.4 eV, the proposed structure is still broadband but exhibits a lower absorptivity. More specifically, the absorptivity of the suggested structure is only 60% when no voltage is supplied to the graphene layer. The adaptable nature of graphene's dynamic tunability empowers the proposed structure to flexibly transition between functioning as an absorber or reflector, offering versatile applications such as electro-optic switches and modulators [52].

This study also delves into exploring the impact of the relaxation time (τ) on the graphene layer, a crucial factor

$$\begin{bmatrix} s_{11} & s_{12} \\ s_{21} & s_{22} \end{bmatrix} = \frac{1}{P_1Z_0 + Q_1 + (R_1Z_0 + S_1)Z_{\text{in}}} \begin{bmatrix} P_1Z_0 + Q_1 - (R_1Z_0 + S_1)Z_{\text{in}} & 2\sqrt{Z_{\text{in}}Z_0} \\ 2\sqrt{Z_{\text{in}}Z_0} & -P_1Z_0 + Q_1 - (R_1Z_0 - S_1)Z_{\text{in}} \end{bmatrix} \qquad (31)$$

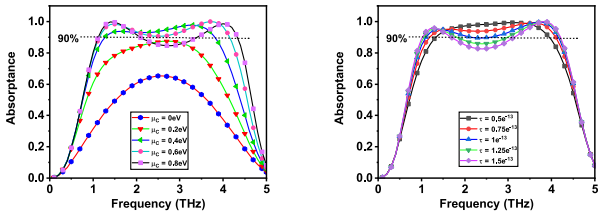

FIGURE 7. Variation in Absorption Spectra: Impact of (a) Various Graphene Chemical Potentials (μ_c) (0-0.8 eV), and (b) Relaxation Time (τ) on the Designed GMMA Structure.

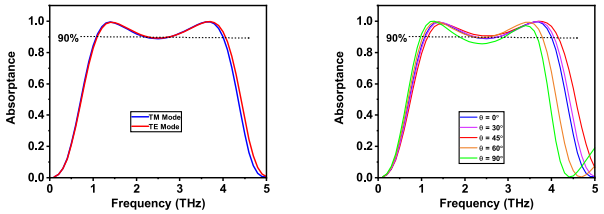

FIGURE 8. (a) Absorptance spectra for TM and TE mode, and (b) Effect of incident angle.

influencing graphene quality [65]. In Fig. 7 (b), we observe a subtle narrowing of the proposed GMMA's bandwidth as τ changes from 0.5×10^{-13} s to 1.5×10^{-13} s, with a step size of 0.25×10^{-13} s. Remarkably, absorptivity consistently exceeds 90% across the entire broadband region in this range. Conversely, an increase in τ results in a reduction in absorptivity at the middle, while the bandwidth remains broad, though with slightly lower absorptivity. Though for $\tau = 0.5e^{-13}$, we get a better absorptivity, but bandwidth is decreased by 0.4 THz. Noteworthy is our decision, based on simulation results, to use $\tau = 1e^{-13}$ because a balance between absorptivity and bandwidth is obtained. It's essential to highlight that variations in τ minimally affect the proposed broadband GMMA's performance, underscoring its resilience to potential fabrication imperfections in the graphene film [52]. In both TE and TM modes, absorptivity exceeds 90%, with the bandwidth slightly higher in the TE mode, as illustrated in Fig. 8 (a). For various incident angles (θ), the absorptivity consistently surpasses 90%, demonstrating the polarization independence of GMMA, as depicted in Fig. 8(b). For $\theta = 45°$, we get the maximum absorptivity and bandwidth. The final absorptance and reflectance spectra are shown in Fig. 9. The bandwidth of the absorptance spectra is around 3 THz (1.14 THz to 4.14 THz), in which absorptivity is over 90%. With absorption values of 99.96% and 98.37% at 1.5 THz and 3.7 THz, respectively, the suggested GMMA shows two distinct absorption peaks.

Additionally, we checked the benefits of our GMMA by comparing it with other graphene-based THz absorbers in Table 2. Our GMMA is designed with a single layer and has a unit cell size of $4.5 \times 4.5\ \mu m^2$. It's easy to make because of its simple design, unlike multi-layer options that are harder

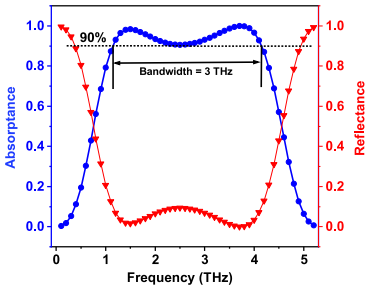

FIGURE 9. Absorptance and Relectance spectra for the proposed GMMA absorber.

TABLE 2. Comparing bandwidth across different GMMA configurations.

References	Year	Constituent Materials	Bandwidth over 90% (THz)	Maximum Absorption
Mou et al. [66]	2018	Graphene, SiO_2, and gold	0.46	>99%
Hu et al. [67]	2020	Graphene, SiO_2, and gold	1.22	>90%
Liu et al. [68]	2020	Graphene, TOPAS, and gold	2.66	>90%
Feng et al. [69]	2021	Graphene, TOPAS, and gold	0.76	99%
Xu et al. [70]	2021	Graphene, SiO_2, and gold	1.16	>99%
Fu et al. [71]	2022	Au, Polyimide, Graphene	1.07	>90%
Huang et al. [72]	2022	Graphene, Polyimide, and gold	2.68	>90%
This paper	2023	Graphene and SiO_2	3	99.96

to implement due to complicated manufacturing and higher costs.

VI. APPLICATION OF GMMA IN ANTENNA

A GMMA antenna is a device that can capture, transform, broadcast, and receive THz EM waves using GMMA structures. GMMA structures are composed of graphene layers patterned into different shapes and sizes, and combined with dielectric and metallic layers, to create various resonant modes and plasmonic effects that enhance the radiation performance of the antenna. THz EM waves can be captured and transformed into electrical signals using broadband THz GMMA devices. In order to broadcast and receive THz signals for wireless communication and data transmission, these devices can also be utilized as antennas. EM wave emitters and receivers are called antennas. Antenna performance is influenced by radiation efficiency, bandwidth, gain, directivity, return loss, insertion loss, and polarization in addition to impedance matching. Enhancing the radiation efficiency and bandwidth of a THz antenna is a problem in antenna design since these parameters are constrained by the high ohmic losses and restricted resonant modes of THz materials and structures. To overcome these obstacles and produce effective, broadband THz antennas, graphene, a two-dimensional material with extraordinary electrical and optical capabilities, can be employed. One possible way to

feed graphene in the system is to use an external voltage bias to modulate the surface conductivity of graphene, which can affect the impedance matching, bandwidth, and polarization of the antenna. Another possible way is to use chemical doping, strain engineering, or external voltages to modify the Fermi energy of graphene, which can affect the plasmonic waves, radiation efficiency, and directivity of the antenna. As a result, graphene can successfully match the impedance of the feed line and the vacant space. Moreover, graphene can support plasmonic waves with a large wave vector and a short wavelength due to its low effective mass and high carrier mobility. This allows graphene to achieve a high radiation efficiency and a wide bandwidth. GMMA can also exhibit negative permittivity and permeability, which enable them to achieve a high directivity and a low backscattering. GMMA can be designed to have a specific polarization or a polarization-independent response. To calculate the gain of an antenna, we typically need more information than just the shape of the antenna and the frequency of the signal. The gain of an antenna depends on various factors, including its size, structure, and the operating frequency. However, we can provide a very basic and rough estimate of the gain by using a common formula for a square aperture antenna. The gain of an antenna can be approximated by the following formula [73]:

$$G \approx \frac{4\pi A_e}{\lambda^2} \tag{39}$$

where G is the gain of the antenna, A_e is the effective aperture of the antenna, and λ is the wavelength of the signal. To calculate the wavelength (λ) at a frequency (f), you can use the formula:

$$\lambda = \frac{c}{f} \tag{40}$$

where c is the speed of light (approximately 3×10^8 meters per second). For our GMMA, effective aperture is 15.1695 μm^2. Let, frequency of the signal is 3 THz, the corresponding wavelength (λ) will be 0.1 mm. The gain (dB) of the GMMA antenna will be 37.78 dB which indicates that the antenna is efficient at directing energy in a specific direction. So, our GMMA antenna with a gain of 37.48 dB is significantly more directional and efficient in focusing its radiated energy compared to a simple omnidirectional antenna. The directivity (D) formula in terms of gain (G) is derived from the basic definition of directivity as the ratio of the maximum radiation intensity of the antenna to the average radiation intensity over all directions. In decibels, it is expressed as:

$$D = 10 \log_{10} \left(\frac{\text{Max Radiation Intensity}}{\text{Average Radiation Intensity}} \right) \tag{41}$$

For an isotropic radiator, the maximum radiation intensity is equal to the average radiation intensity, resulting in a directivity of 1 (0 dB). When expressing directivity in terms of gain, the formula becomes [73]:

$$D = G - 10 \log_{10}(4\pi) \tag{42}$$

The directivity of the GMMA antenna will be 32.81 dB which indicates that the GMMA antenna is able to concentrate its radiation in a specific direction more effectively than an isotropic radiator. This can be desirable in applications where you want to maximize signal strength or minimize interference from specific directions. Return loss (RL) serves as a metric for assessing the degree to which a device or component aligns with the impedance of the connected system. This parameter is expressed in decibels (dB) and is computed using the formula:

$$RL = -20 \log_{10}(|S_{11}|) \tag{43}$$

Here, S_{11} is the reflection coefficient. In our case, the maximum return loss of GMMA antenna is -34 dB, shown in Fig. 10 (a). This value signifies a remarkably effective impedance matching within the system, suggesting that a substantial portion of the incident power is efficiently transmitted without undue reflection back towards the source. A higher return loss value indicates superior impedance matching, implying reduced reflection of power. The efficiency (η) of

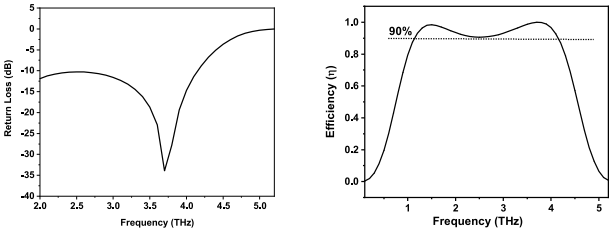

FIGURE 10. (a) Return loss, and (b) efficiency of the GMMA antenna.

an antenna is often related to its reflection coefficient (S_{11}) and transmission coefficient (S_{21}). The efficiency can be expressed in terms of these parameters as follows:

$$\eta = 1 - |S_{11}|^2 - |S_{21}|^2 \tag{44}$$

Here, η is the antenna efficiency, and S_{21} is the transmission coefficient. The efficiency is essentially a measure of how well an antenna converts the input power into radiated power, accounting for both reflected and transmitted power. In analyzing Fig. 10 (b), the GMMA antenna demonstrates remarkable efficiency exceeding 0.9, with a peak value reaching an impressive 0.9996. The antenna operates in the THz region, which is a very high frequency range from 0.1 to 10 THz. The structure of the antenna is kind of rectangular patch antenna, which is a common type of antenna for THz applications. The patch can be excited by various methods, such as a microstrip line, a coaxial probe, or a slot. The model of our proposed antenna can further develop like Coaxial-fed rectangular patch antenna. Our proposed antenna design consists of three distinct layers: the metasurface layer, the driven patch layer, and the feeding network layer [74]. These layers can be implemented on two RO4350 substrates and a TLY-5 substrate, as illustrated in Fig. 11, and the connection between the driven patch layer and the feeding network layer is established through the utilization of a RO4450 substrate [74].

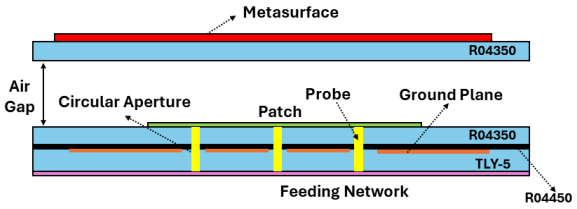

FIGURE 11. Suggested Antenna Model Design.

The comprehensive performance evaluation presented in Table 3 establishes a clear superiority of the proposed GMMA antenna across various parameters when compared to other antenna models. Notably, the GMMA antenna excels in gain, directivity, return loss, and efficiency, surpassing counterparts detailed in Table 3. With a gain of 37.48 dB, the GMMA antenna surpasses conventional antennas, which typically have gains below 10 dB, achieving almost four times better performance. Its directivity of 32.81 dB indicates focused power radiation, reducing interference from external sources. The antenna also demonstrates a notable return loss of -34 dB, suggesting excellent impedance matching and minimal reflection of input power. Importantly, the GMMA antenna achieves an outstanding maximum efficiency of 99.96%, surpassing all other models. This highlights its exceptional capability to convert nearly all input power into radiated power with minimal losses.

TABLE 3. Comparison of antenna performance parameters.

References	Year	Methodology	Max Gain (dB)	Max Efficiency (%)
Liu et al. [75]	2015	ENG-TL	3.42	86.2
Khan et al. [76]	2016	CSRR	4.7	82
Sharma et al. [64]	2015	ZOR	1.59	91.5
Han et al. [77]	2015	Meandered PIFA	1.26	74.19
Gupta et al. [78]	2017	CRLH, SRR	1.05, 2.59	98.5, 97.2
Jagtap et al. [79]	2018	RIS and PRS	12.5	-
Rao et al. [80]	2018	CSRR	7	-
Jafargholi et al. [81]	2018	Complimentary capacitively loaded loop	4	>95
Shaw et al. [82]	2018	CSRR and MTM slab	-0.6	84.2
Kumar et al. [83]	2018	ENG-TL concentric closed ring resonator	1.59, 2.1, 4.97	73.82, 95
Hong et al. [84]	2019	FSS	-	-
Gupta et al. [85]	2019	Elliptical shaped SRR	-	83.33, 99.38
Wang et al. [86]	2020	SRR and CRLH-TL	5.4	74
Gudibandi et al. [87]	2020	High refractive index	-1.4	-
This paper	2023	GMMA	37.48	99.96

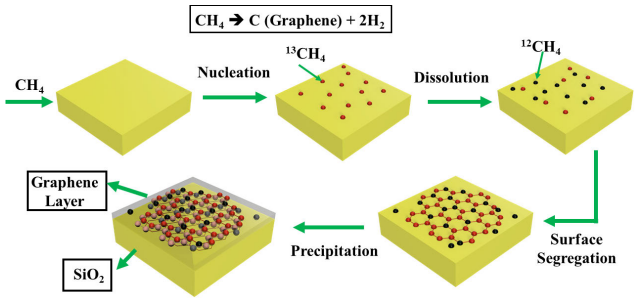

FIGURE 12. Possible fabrication process of GMMA.

VII. POSSIBLE FABRICATION PROCESS

The fabrication of the proposed device involves a multi-step process, illustrated in Fig. 12, primarily relying on the chemical vapor deposition (CVD) technique, known for its cost-effectiveness and reliability. The key material in this process is graphene, a single layer of carbon atoms arranged in a hexagonal lattice structure, chosen for its exceptional properties. To initiate the fabrication, graphene is grown as a high-quality single layer on a copper or nickel substrate using the CVD technique [88]. This step ensures the production of a pristine graphene layer, crucial for the device's performance. The choice of copper or nickel as substrates provides a suitable surface for graphene growth while maintaining affordability. Once the graphene layer is grown, it is transferred onto the dielectric material, in this case, SiO_2. Furthermore, the adaptability of the production method may be increased by transferring the graphene generated by CVD to a variety of other substrates [89]. This stage enables modification according to particular substrate preferences or application needs. Spin coating is used to place a thin dielectric layer over the structure after the graphene transfer. The dielectric substance is distributed uniformly by spin coating, and the structure is then hardened in a vacuum oven. The dielectric layer is strengthened throughout this curing process, providing a strong basis for the next graphene layers. We repeat the CVD procedure for the subsequent graphene layer. Like in the first stage, a new sheet of graphene is generated on a copper substrate and then placed on top of the preexisting structure. Next, using the spin coating method, the dielectric layer is applied to this newly created graphene sheet and allowed to cure in a vacuum oven. The development of a strong and efficient device structure is ensured by this stacking process. A regular lithography procedure is used to produce the top graphene pattern in the last phase of the manufacturing process [90]. This thorough production process, which demonstrates the strategic integration of materials and procedures for maximum performance, provides the groundwork for the successful creation of the proposed device.

VIII. CONCLUSION

This paper introduces an innovative design for a graphene-based metamaterial absorber (GMMA) that exhibits the

ability to absorb over 90% of EM waves across a broad frequency range (1.14-4.14 THz), irrespective of polarization. The theoretical framework for analyzing this structure is presented through the application of transmission line theory and the use of a transmission matrix. This approach further expands the understanding of the relationship between input impedance and reflection coefficient. The GMMA displays several remarkable features such as tunability, polarization independence, and robustness against structural changes. These characteristics make the GMMA an excellent contender for various applications within the THz range. The tunable and broadband capabilities demonstrated in this study significantly enhance the development of GMMA technology specifically designed for THz frequencies. Furthermore, the structure's exceptional clarity and simplicity make it ideally suited for antenna applications. To sum up, the GMMA's versatility and adaptability position it as a valuable tool in addressing the challenges and requirements of pioneering innovations in the THz spectrum. This research not only contributes to the advancement of GMMA technology but also opens up new possibilities for its practical applications.

ACKNOWLEDGMENT

The authors would like to thank the Department of Electrical and Electronic Engineering, BRAC University for their valuable support throughout the research.

DISCLOSURES

The authors declare no conflicts of interest.

SUPPLEMENTAL DOCUMENT

See Supplement 1 for supporting content.

REFERENCES

[1] J. Hao, J. Wang, X. Liu, W. J. Padilla, L. Zhou, and M. Qiu, "High performance optical absorber based on a plasmonic metamaterial," *Appl. Phys. Lett.*, vol. 96, no. 25, 2010, Art. no. 251104.

[2] D. Schurig, J. J. Mock, B. J. Justice, S. A. Cummer, J. B. Pendry, A. F. Starr, and D. R. Smith, "Metamaterial electromagnetic cloak at microwave frequencies," *Science*, vol. 314, no. 5801, pp. 977–980, Nov. 2006.

[3] R. M. Walser, "Electromagnetic metamaterials," in *Complex Mediums II: Beyond Linear Isotropic Dielectrics*, vol. 4467. Bellingham, WA, USA: SPIE, 2001, pp. 1–15.

[4] P. Zamzam, P. Rezaei, Y. I. Abdulkarim, and O. Mohsen Daraei, "Graphene-based polarization-insensitive metamaterials with perfect absorption for terahertz biosensing applications: Analytical approach," *Opt. Laser Technol.*, vol. 163, Aug. 2023, Art. no. 109444.

[5] J. Zhao, S. Wei, C. Wang, K. Chen, B. Zhu, T. Jiang, and Y. Feng, "Broadband microwave absorption utilizing water-based metamaterial structures," *Opt. Exp.*, vol. 26, no. 7, pp. 8522–8531, 2018.

[6] M. Islam, J. Sultana, M. Biabanifard, Z. Vafapour, M. Nine, A. Dinovitser, C. Cordeiro, B.-H. Ng, and D. Abbott, "Tunable localized surface plasmon graphene metasurface for multiband superabsorption and terahertz sensing," *Carbon*, vol. 158, pp. 559–567, Mar. 2020.

[7] Z. Song, K. Wang, J. Li, and Q. H. Liu, "Broadband tunable terahertz absorber based on vanadium dioxide metamaterials," *Opt. Exp.*, vol. 26, no. 6, pp. 7148–7154, 2018.

[8] M. Manjappa, Y. K. Srivastava, A. Solanki, A. Kumar, T. C. Sum, and R. Singh, "Hybrid lead halide perovskites for ultrasensitive photoactive switching in terahertz metamaterial devices," *Adv. Mater.*, vol. 29, no. 32, Aug. 2017, Art. no. 1605881.

[9] Z. Zhou, S. Wang, Y. Yu, Y. Chen, and L. Feng, "High performance metamaterials-high electron mobility transistors integrated terahertz modulator," *Opt. Exp.*, vol. 25, no. 15, pp. 17832–17840, 2017.

[10] J.-Y. Gao, J. Liu, H.-M. Yang, H.-S. Liu, G. Zeng, and B. Huang, "Anisotropic medium sensing controlled by bound states in the continuum in polarization-independent metasurfaces," *Opt. Exp.*, vol. 31, no. 26, pp. 44703–44719, 2023.

[11] M. A. Baqir and P. K. Choudhury, "Hyperbolic metamaterial-based optical biosensor for detecting cancer cells," *IEEE Photon. Technol. Lett.*, vol. 35, no. 4, pp. 183–186, Feb. 2023.

[12] Y. I. Abdulkarim, A. Mohanty, O. P. Acharya, B. Appasani, M. S. Khan, S. K. Mohapatra, F. F. Muhammadsharif, and J. Dong, "A review on metamaterial absorbers: Microwave to optical," *Frontiers Phys.*, vol. 10, Apr. 2022, Art. no. 893791.

[13] R. A. Shelby, D. R. Smith, and S. Schultz, "Experimental verification of a negative index of refraction," *Science*, vol. 292, no. 5514, pp. 77–79, Apr. 2001.

[14] J. B. Pendry, "Negative refraction makes a perfect lens," *Phys. Rev. Lett.*, vol. 85, no. 18, pp. 3966–3969, Oct. 2000.

[15] D. R. Smith, W. J. Padilla, D. C. Vier, S. C. Nemat-Nasser, and S. Schultz, "Composite medium with simultaneously negative permeability and permittivity," *Phys. Rev. Lett.*, vol. 84, no. 18, pp. 4184–4187, May 2000.

[16] N. I. Landy, S. Sajuyigbe, J. J. Mock, D. R. Smith, and W. J. Padilla, "Perfect metamaterial absorber," *Phys. Rev. Lett.*, vol. 100, no. 20, May 2008, Art. no. 207402.

[17] S. Tan, F. Yan, W. Wang, H. Zhou, and Y. Hou, "Ultrasensitive sensing with three-dimensional terahertz metamaterial absorber," *J. Opt.*, vol. 20, no. 5, May 2018, Art. no. 055101.

[18] A. Ishikawa and T. Tanaka, "Metamaterial absorbers for infrared detection of molecular self-assembled monolayers," *Sci. Rep.*, vol. 5, no. 1, p. 12570, Jul. 2015.

[19] Y. Xie, X. Fan, Y. Chen, J. D. Wilson, R. N. Simons, and J. Q. Xiao, "A subwavelength resolution microwave/6.3 GHz camera based on a metamaterial absorber," *Sci. Rep.*, vol. 7, no. 1, p. 40490, Jan. 2017.

[20] Q.-Y. Wen, Y.-S. Xie, H.-W. Zhang, Q.-H. Yang, Y.-X. Li, and Y.-L. Liu, "Transmission line model and fields analysis of metamaterial absorber in the terahertz band," *Opt. Exp.*, vol. 17, no. 22, pp. 20256–20265, 2009.

[21] A. Sobhani, M. W. Knight, Y. Wang, B. Zheng, N. S. King, L. V. Brown, Z. Fang, P. Nordlander, and N. J. Halas, "Narrowband photodetection in the near-infrared with a plasmon-induced hot electron device," *Nature Commun.*, vol. 4, no. 1, p. 1643, Mar. 2013.

[22] M. Huang, Y. Cheng, Z. Cheng, H. Chen, X. Mao, and R. Gong, "Based on graphene tunable dual-band terahertz metamaterial absorber with wide-angle," *Opt. Commun.*, vol. 415, pp. 194–201, May 2018.

[23] R. Degl'Innocenti, H. Lin, and M. Navarro-Cía, "Recent progress in terahertz metamaterial modulators," *Nanophotonics*, vol. 11, no. 8, pp. 1485–1514, May 2022.

[24] X. Li, Q. Li, L. Wu, Z. Xu, and J. Yao, "Focusing on the development and current status of metamaterial absorber by bibliometric analysis," *Materials*, vol. 16, no. 6, p. 2286, Mar. 2023.

[25] X. Cai, R. Tang, H. Zhou, Q. Li, S. Ma, D. Wang, T. Liu, X. Ling, W. Tan, Q. He, S. Xiao, and L. Zhou, "Dynamically controlling terahertz wavefronts with cascaded metasurfaces," *Adv. Photon.*, vol. 3, no. 3, Jun. 2021, Art. no. 036003.

[26] W. Choi, I. Lahiri, R. Seelaboyina, and Y. S. Kang, "Synthesis of graphene and its applications: A review," *Crit. Rev. Solid State Mater. Sci.*, vol. 35, no. 1, pp. 52–71, 2010.

[27] H. A. Murthy, S. Ghotekar, B. Vinay Kumar, and A. Roy, "Graphene: A multifunctional nanomaterial with versatile applications," *Adv. Mater. Sci. Eng.*, vol. 2021, Dec. 2021, Art. no. 2418149.

[28] G. Varshney and P. Giri, "Bipolar charge trapping for absorption enhancement in a graphene-based ultrathin dual-band terahertz biosensor," *Nanosc. Adv.*, vol. 3, no. 20, pp. 5813–5822, 2021.

[29] M. Zhong, S. Li, Y. Zou, H. Fan, Y. Jiang, C. Qiu, J. Luo, and L. Yang, "Hydrophobic surface array structure based on laser-induced graphene for deicing and anti-icing applications," *Micromachines*, vol. 15, no. 2, p. 285, Feb. 2024.

[30] M. A. Baqir, P. K. Choudhury, T. Fatima, and A.-B.-M. A. Ibrahim, "Graphene-over-graphite-based metamaterial structure as optical filter in the visible regime," *Optik*, vol. 180, pp. 832–839, Feb. 2019.

[31] W. B. Lu, J. W. Wang, J. Zhang, Z. G. Liu, H. Chen, W. J. Song, and Z. H. Jiang, "Flexible and optically transparent microwave absorber with wide bandwidth based on graphene," *Carbon*, vol. 152, pp. 70–76, Nov. 2019.

[32] X. Huang, W. He, F. Yang, J. Ran, B. Gao, and W.-L. Zhang, "Polarization-independent and angle-insensitive broadband absorber with a target-patterned graphene layer in the terahertz regime," *Opt. Exp.*, vol. 26, no. 20, pp. 25558–25566, 2018.
[33] S. Liao, J. Sui, and H. Zhang, "Switchable ultra-broadband absorption and polarization conversion metastructure controlled by light," *Opt. Exp.*, vol. 30, no. 19, pp. 34172–34187, 2022.
[34] Y. Li, L. Zeng, H. Zhang, D. Zhang, K. Xia, and L. Zhang, "Multifunctional and tunable metastructure based on VO_2 for polarization conversion and absorption," *Opt. Exp.*, vol. 30, no. 19, pp. 34586–34600, 2022.
[35] H. Pan and H. Zhang, "Broadband polarization-insensitive coherent rasorber in terahertz metamaterial with enhanced anapole response and coupled toroidal dipole modes," *Adv. Opt. Mater.*, vol. 10, no. 2, Jan. 2022, Art. no. 2101688.
[36] H. Pan, B.-X. Li, and H. F. Zhang, "Anapole-excited terahertz multifunctional spoof surface plasmon polariton directional Janus metastructures," *Phys. Chem. Chem. Phys.*, vol. 25, no. 16, pp. 11375–11386, 2023.
[37] Y. Ma and H. Zhang, "Wide-angle energy steering and magnetic information detection-coding of stacked ferrite-based elements in the gradient magnetic domain," *Opt. Laser Technol.*, vol. 156, Dec. 2022, Art. no. 108544.
[38] Z. Xu, D. Wu, Y. Liu, C. Liu, Z. Yu, L. Yu, and H. Ye, "Design of a tunable ultra-broadband terahertz absorber based on multiple layers of graphene ribbons," *Nanosc. Res. Lett.*, vol. 13, no. 1, pp. 1–8, Dec. 2018.
[39] W. X. Lim and R. Singh, "Universal behaviour of high-Q Fano resonances in metamaterials: Terahertz to near-infrared regime," *Nano Converg.*, vol. 5, no. 1, pp. 1–7, Dec. 2018.
[40] Y. Wang, Z. Yang, H. Wang, E. Li, and Y. Yuan, "Investigation of PTFE-based ultra-low dielectric constant composite substrates with hollow silica ceramics," *J. Mater. Sci., Mater. Electron.*, vol. 33, no. 7, pp. 4550–4558, Mar. 2022.
[41] A. Khan and R. Nema, "Analysis of five different dielectric substrates on microstrip patch antenna," *Int. J. Comput. Appl.*, vol. 55, no. 14, pp. 40–47, Oct. 2012.
[42] N. R. Sabaruddin, Y. M. Tan, S.-H. Chen, C.-T. Chou Chao, C. M. Lim, R. Thotagamuge, M. R. R. Kooh, and Y.-F. Chou Chau, "Designing a broadband terahertz metamaterial absorber through bi-layer hybridization of metal and graphene," *Plasmonics*, pp. 1–4, Feb. 2024.
[43] P. Kokkonen, A. Beier, S. Mazurenko, J. Damborsky, D. Bednar, and Z. Prokop, "Substrate inhibition by the blockage of product release and its control by tunnel engineering," *RSC Chem. Biol.*, vol. 2, no. 2, pp. 645–655, 2021.
[44] C. S. R. Kaipa, A. B. Yakovlev, G. W. Hanson, Y. R. Padooru, F. Medina, and F. Mesa, "Enhanced transmission with a graphene-dielectric microstructure at low-terahertz frequencies," *Phys. Rev. B, Condens. Matter*, vol. 85, no. 24, Jun. 2012, Art. no. 245407.
[45] V. P. Gusynin, S. G. Sharapov, and J. P. Carbotte, "Magneto-optical conductivity in graphene," *J. Phys., Condens. Matter*, vol. 19, no. 2, Jan. 2007, Art. no. 026222.
[46] V. P. Gusynin, S. G. Sharapov, and J. P. Carbotte, "Sum rules for the optical and Hall conductivity in graphene," *Phys. Rev. B, Condens. Matter*, vol. 75, no. 16, Apr. 2007, Art. no. 165407.
[47] G. W. Hanson, "Dyadic Green's functions and guided surface waves for a surface conductivity model of graphene," *J. Appl. Phys.*, vol. 103, no. 6, 2008, Art. no. 064302.
[48] A. Beheshti Asl, D. Pourkhalil, A. Rostami, and H. Mirtaghioglu, "A perfect electrically tunable graphene-based metamaterial absorber," *J. Comput. Electron.*, vol. 20, no. 2, pp. 864–872, Apr. 2021.
[49] R. Mishra, R. Panwar, and D. Singh, "Equivalent circuit model for the design of frequency-selective, terahertz-band, graphene-based metamaterial absorbers," *IEEE Magn. Lett.*, vol. 9, 2018, Art. no. 3707205.
[50] L. Ye, F. Zeng, Y. Zhang, and Q. H. Liu, "Composite graphene-metal microstructures for enhanced multiband absorption covering the entire terahertz range," *Carbon*, vol. 148, pp. 317–325, Jul. 2019.
[51] N. T. Q. Hoa, T. S. Tuan, L. T. Hieu, and B. L. Giang, "RETRACTED ARTICLE: Facile design of an ultra-thin broadband metamaterial absorber for C-band applications," *Sci. Rep.*, vol. 9, no. 1, p. 468, Jan. 2019.
[52] X. Du, F. Yan, W. Wang, S. Tan, L. Zhang, Z. Bai, H. Zhou, and Y. Hou, "A polarization- and angle-insensitive broadband tunable metamaterial absorber using patterned graphene resonators in the terahertz band," *Opt. Laser Technol.*, vol. 132, Dec. 2020, Art. no. 106513.
[53] S. Asgari and T. Fabritius, "Graphene-based multiband chiral metamaterial absorbers comprised of square split-ring resonator arrays with different numbers of gaps, and their equivalent circuit model," *IEEE Access*, vol. 10, pp. 63658–63671, 2022.
[54] L. Sun, J. Sun, B. Yang, X. Gao, H. Long, and Y. Shao, "A simplified design of broadband metamaterial absorber covering X- and Ku- band," *Mater. Res. Exp.*, vol. 6, no. 12, Jan. 2020, Art. no. 125805.
[55] D. R. Smith and D. Schurig, "Electromagnetic wave propagation in media with indefinite permittivity and permeability tensors," *Phys. Rev. Lett.*, vol. 90, no. 7, Feb. 2003, Art. no. 077405.
[56] I. Chaharmahali, M. Soltani, M. Hoseini, and M. Biabanifard, "Control of terahertz waves for TE and TM modes using graphene-based metamaterials," *Opt. Eng.*, vol. 59, no. 4, 2020, Art. no. 047101.
[57] M.-R. Nickpay, M. Danaie, and A. Shahzadi, "Graphene-based metamaterial absorber for refractive index sensing applications in terahertz band," *Diamond Rel. Mater.*, vol. 130, Dec. 2022, Art. no. 109539.
[58] M.-R. Nickpay, M. Danaie, and A. Shahzadi, "Design of a graphene-based multi-band metamaterial perfect absorber in THz frequency region for refractive index sensing," *Phys. E: Low-Dimensional Syst. Nanostruct.*, vol. 138, Apr. 2022, Art. no. 115114.
[59] Z. Wu, J. Tian, and R. Yang, "A graphene based dual-band metamaterial absorber for TE polarized THz wave," *Micro Nanostruct.*, vol. 168, Aug. 2022, Art. no. 207331.
[60] D. M. Pozar, *Microwave Engineering*. Hoboken, NJ, USA: Wiley, 2011.
[61] E. Chung, J.-I. Ha, A. A. Bastami, and D. J. Perreault, "Impedance compressing matching network based on two-port network analysis for wireless power transfer system," *IEEE J. Emerg. Sel. Topics Ind. Electron.*, vol. 3, no. 3, pp. 432–442, Jul. 2022.
[62] A. Izadian, "Two-port networks," in *Fundamentals of Modern Electric Circuit Analysis and Filter Synthesis: A Transfer Function Approach*. Cham, Switzerland: Springer, 2023, pp. 609–669.
[63] D. F. Bowman, "Impedance matching and broadbanding," in *Antenna Engineering Handbook*, vol. 2, 1961, pp. 2–43.
[64] S. K. Sharma, A. Gupta, and R. K. Chaudhary, "Epsilon negative CPW-fed zeroth-order resonating antenna with backed ground plane for extended bandwidth and miniaturization," *IEEE Trans. Antennas Propag.*, vol. 63, no. 11, pp. 5197–5203, Nov. 2015.
[65] A. Arsanjani, M. Biabanifard, and M. S. Abrishamian, "A novel analytical method for designing a multi-band, polarization-insensitive and wide angle graphene-based THz absorber," *Superlattices Microstruct.*, vol. 128, pp. 157–169, Apr. 2019.
[66] N. Mou, S. Sun, H. Dong, S. Dong, Q. He, L. Zhou, and L. Zhang, "Hybridization-induced broadband terahertz wave absorption with graphene metasurfaces," *Opt. Exp.*, vol. 26, no. 9, pp. 11728–11736, 2018.
[67] D. Hu, T. Meng, H. Wang, and Y. Ma, "Tunable broadband terahertz absorber based on plasmon hybridization in monolayer graphene ring arrays," *Appl. Opt.*, vol. 59, no. 35, pp. 11053–11058, 2020.
[68] L. Liu, W. Liu, and Z. Song, "Ultra-broadband terahertz absorber based on a multilayer graphene metamaterial," *J. Appl. Phys.*, vol. 128, no. 9, 2020, Art. no. 093104.
[69] H. Feng, Z. Xu, K. Li, M. Wang, W. Xie, Q. Luo, B. Chen, W. Kong, and M. Yun, "Tunable polarization-independent and angle-insensitive broadband terahertz absorber with graphene metamaterials," *Opt. Exp.*, vol. 29, no. 5, pp. 7158–7167, 2021.
[70] J. Xu, Z. Qin, M. Chen, Y. Cheng, H. Liu, R. Xu, C. Teng, S. Deng, H. Deng, H. Yang, S. Qu, and L. Yuan, "Broadband tunable perfect absorber with high absorptivity based on double layer graphene," *Opt. Mater. Exp.*, vol. 11, no. 10, pp. 3398–3410, 2021.
[71] M. Fu, J. Wang, S. Guo, Z. Wang, P. Yang, and Y. Niu, "A polarization-insensitive broadband terahertz absorber using patterned graphene," *Nanomaterials*, vol. 12, no. 21, p. 3763, Oct. 2022.
[72] X. Huang, M. Cao, D. Wang, X. Li, J. Fan, and X. Li, "Broadband polarization-insensitive and oblique-incidence terahertz metamaterial absorber with multi-layered graphene," *Opt. Mater. Exp.*, vol. 12, no. 2, pp. 811–822, 2022.
[73] C. A. Balanis, *Antenna Theory: Analysis and Design*. Hoboken, NJ, USA: Wiley, 2016.
[74] J. Hu, G. Q. Luo, and Z.-C. Hao, "A wideband quad-polarization reconfigurable metasurface antenna," *IEEE Access*, vol. 6, pp. 6130–6137, 2018.
[75] L.-Y. Liu and B.-Z. Wang, "A broadband and electrically small planar monopole employing metamaterial transmission line," *IEEE Antennas Wireless Propag. Lett.*, vol. 14, pp. 1018–1021, 2015.
[76] M. S. Khan, A.-D. Capobianco, S. M. Asif, D. E. Anagnostou, R. M. Shubair, and B. D. Braaten, "A compact CSRR-enabled UWB diversity antenna," *IEEE Antennas Wireless Propag. Lett.*, vol. 16, pp. 808–812, 2017.

[77] K. Han, M. Swaminathan, R. Pulugurtha, H. Sharma, R. Tummala, S. Yang, and V. Nair, "Magneto-dielectric nanocomposite for antenna miniaturization and SAR reduction," *IEEE Antennas Wireless Propag. Lett.*, vol. 15, pp. 72–75, 2016.
[78] A. Gupta and R. K. Chaudhary, "A miniaturized dual-band ZOR antenna using epsilon negative transmission line loading," *Int. J. Microw. Wireless Technol.*, vol. 9, no. 8, pp. 1735–1739, Oct. 2017.
[79] S. Jagtap, A. Chaudhari, N. Chaskar, S. Kharche, and R. K. Gupta, "A wideband microstrip array design using RIS and PRS layers," *IEEE Antennas Wireless Propag. Lett.*, vol. 17, pp. 509–512, 2018.
[80] P. H. Rao, J. S. Sajin, and K. Kudesia, "Miniaturisation of switched beam array antenna using phase delay properties of CSRR-loaded transmission line," *IET Microw., Antennas Propag.*, vol. 12, no. 12, pp. 1960–1966, Oct. 2018.
[81] A. Jafargholi and A. Jafargholi, "Miniaturisation of printed slot antennas using artificial magnetic conductors," *IET Microw., Antennas Propag.*, vol. 12, no. 7, pp. 1054–1059, Jun. 2018.
[82] T. Shaw and D. Mitra, "Efficient design of electrically small antenna using metamaterials for wireless applications," *CSI Trans. ICT*, vol. 6, no. 1, pp. 51–58, Mar. 2018.
[83] R. Kumar, R. Singh, and R. K. Chaudhary, "Miniaturised triple-band antenna loaded with complementary concentric closed ring resonators with asymmetric coplanar waveguide-fed based on epsilon negative transmission line," *IET Microw., Antennas Propag.*, vol. 12, no. 13, pp. 2073–2079, Oct. 2018.
[84] T. Hong, M. Wang, K. Peng, and S. Gong, "Ultrathin and miniaturized frequency selective surface with closely located dual resonance," *IEEE Antennas Wireless Propag. Lett.*, vol. 18, pp. 1288–1292, 2019.
[85] A. Gupta and R. Kumar Singh, "A miniaturized elliptically shaped split ring resonator antenna with dual-band characteristics," in *Advances in Signal Processing and Communication (ICSC)*. Singapore: Springer, 2019, pp. 37–44.
[86] Z. Wang, Y. Dong, and T. Itoh, "Miniaturized wideband CP antenna based on metaresonator and CRLH-TLs for 5G new radio applications," *IEEE Trans. Antennas Propag.*, vol. 69, no. 1, pp. 74–83, Jan. 2021.
[87] B. R. Gudibandi, H. A. Murugan, and S. K. Dhamodharan, "Miniaturization of monopole antenna using high refractive index metamaterial loading," *Int. J. RF Microw. Comput.-Aided Eng.*, vol. 30, no. 5, May 2020, Art. no. e22163.
[88] E. Rezagholizadeh, M. Biabanifard, and S. Borzooei, "Analytical design of tunable THz refractive index sensor for TE and TM modes using graphene disks," *J. Phys. D, Appl. Phys.*, vol. 53, no. 29, Jul. 2020, Art. no. 295107.
[89] Y. Hao, M. S. Bharathi, L. Wang, Y. Liu, H. Chen, S. Nie, X. Wang, H. Chou, C. Tan, B. Fallahazad, H. Ramanarayan, C. W. Magnuson, E. Tutuc, B. I. Yakobson, K. F. McCarty, Y.-W. Zhang, P. Kim, J. Hone, L. Colombo, and R. S. Ruoff, "The role of surface oxygen in the growth of large single-crystal graphene on copper," *Science*, vol. 342, no. 6159, pp. 720–723, Nov. 2013.
[90] M. D. Astorino, R. Fastampa, F. Frezza, L. Maiolo, M. Marrani, M. Missori, M. Muzi, N. Tedeschi, and A. Veroli, "Polarization-maintaining reflection-mode THz time-domain spectroscopy of a polyimide based ultra-thin narrow-band metamaterial absorber," *Sci. Rep.*, vol. 8, no. 1, p. 1985, Jan. 2018.

RUMMANUR RAHAD (Member, IEEE) received the B.Sc. degree in electrical and electronic engineering from Islamic University of Technology (IUT), Gazipur, Bangladesh, in 2023. He is currently a Research Assistant with the Optics and Photonics Research Group, BRAC University, Bangladesh. He is also a part-time Lecturer with IUT. He has authored several research articles in renowned journals, such as *Optics Express*, *Results in Physics*, *Sensing and Bio-sensing Research*, and *Optics Communications*. His research interests include optical devices, metamaterials, IB solar cells, and quantum optics.

ABU S. M. MOHSIN (Member, IEEE) received the B.Sc. degree in electrical and electronics engineering (EEE) from Islamic University of Technology (IUT), Gazipur, Dhaka, in November 2008, and the Ph.D. degree in nanotechnology/nano-bio-photonics from the Swinburne University of Technology, Australia, in December 2015. From 2009 to 2011, he was a Lecturer with the Department of Electrical and Electronic Engineering, Stamford University Bangladesh. From 2011 to 2018, he was worked for several department with the Swinburne University of Technology in different capacities. He was a multidisciplinary research Scientist at the interface of engineering, physics and biology. His research interests include nano-bio-photonics, plasmonic nanomaterial and its application, single particle microspectroscopy, nanoparticle cell interaction and live cell imaging, renewables, embedded system design, automation, control, and the IoT.

MOHAMMED BELAL HOSSAIN BHUIAN received the Bachelor of Science degree in electrical and electronic engineering from Bangladesh University of Engineering and Technology (BUET), in 1998, the M.Eng. degree from Dublin City University, Ireland, in 2002, and the Ph.D. degree from Tyndall National Institute, University College Cork, Ireland, in 2008. He spent one year as a Postdoctoral Researcher with Laser Zentrum Hannover e.V., Hannover, Germany. He joined BRAC University, Bangladesh, as an Assistant Professor, in 2010, where he is currently an Associate Professor with the Department of Electrical and Electronic Engineering. His research interest includes femtosecond laser mediated micro/nanofabrication of polymer based structures for different applications. He has gained extensive research experience on a range of topics related to optics and photonics, such as the design and development of a laser based optical system, fabrication of microstructures, beam shape engineering using both diffractive and refractive optics, fabrication, and characterization of plasmonics microstructure.

MD. MOSADDEQUR RAHMAN received the Graduate degree from the Electrical and Electronic Engineering Department, Bangladesh University of Engineering and Technology (BUET), in 1991, and the Doctor of Engineering (Electrical) degree from Nagoya Institute of Technology (NIT), Nagoya, Japan, in 1999. He was a Faculty Member of BUET, from 1991 to 1993, and King Fahd University of Petroleum and Minerals (KFUPM), Saudi Arabia, from 2001 to 2005, and a Visiting Lecturer with NIT, from 1999 to 2001. He was also involved with the research and development of micro-electromechanical systems (MEMS)-based ultrasonic sensors and actuators with the University of Windsor, Windsor, Canada, from 2008 to 2009. Currently, he is a Professor with the Department of Electrical and Electronic Engineering, BRAC University, Dhaka, Bangladesh. He has extensive experience in the growth and characterization of semiconducting thin films and device fabrication techniques, design, analysis and modeling of opto-electronic semiconductor materials and devices, micro-electro-mechanical systems (MEMS)-based devices, sensors, and signal conditioning circuits. He has published over 50 scientific papers in internationally reputed journals and conference proceedings. His research interests include solar energy materials and solar cells, photovoltaic systems, novel and low-cost semiconducting thin film materials for opto-electronic device application, and micro-electromechanical systems (MEMS)-based sensors and actuators. He is a registered professional engineer (P.Eng.) in the province of Ontario.